Pre-print submitted version

Deposition Kinetics and Compositional Control of Vacuum Processed $CH_3NH_3PbI_3$ Perovskite

Beom-Soo Kim, Lidón Gil-Escrig, Michele Sessolo and Henk J. Bolink*.*

Instituto de Ciencia Molecular, Universidad de Valencia, Calle Catedrático Jose Beltrán 2, Paterna, 46980, Spain.

Corresponding Author: beom.kim@uv.es, henk.bolink@uv.es

Abstract

Halide perovskites have generated considerable research interest due to their excellent optoelectronic properties in the past decade. To ensure the formation of high quality semiconductors, the deposition process for the perovskite film is a critical issue. Vacuum based processing is considered a promising method allowing, in principle, also for large areas. One of the benefits of vacuum processing is the control over the film composition through the use of quartz crystal microbalances (QCMs) that in-situ monitor the rates of the components. In metal halide perovskites, however, one frequently employed component or precursor, CH_3NH_3I, exhibits non-standard sublimation properties. Here, we study in detail the sublimation properties of CH_3NH_3I and demonstrate that by correcting for its complex adsorption properties and by modeling the film growth, accurate predictions about the stoichiometry of the final perovskite film can be obtained.

Metal halide perovskite have attracted tremendous attentions as an emerging material for energy harvesting due to their outstanding optoelectronic properties, featured as rapid increase in power conversion efficiency (PCE) of solar cells from 3.9% to 25.2% in last 10 years [1-3]. In this field, growing a high-quality film has been one of the most challenging and important issues. This as the device performance is directly related to the quality (crystallization, morphology, density of defects in the bulk or the surface) of the perovskite film. The deposition method used to prepare the perovskite film has a large influence on its quality and therefore also on the device performance. Therefore, the fabrication process for the perovskite films have been extensively studied to improve the film and device properties. Perovskite thin film deposition started by using one-step spin coating, and was followed by a variety of alternative approaches such as sequential deposition, solvent engineering, and solvent assisted vapor process or hybrid process [4-11]. Current thin film deposition efforts focus on the compatibility with large area and high throughputs. One widely accepted processing method in semiconductor industry is thermal vacuum deposition, or sublimation. This has been demonstrated successfully in the organic light-emitting diodes (OLEDs) industry. The vacuum process is particularly suited for manufacturing optoelectronic devices since high purity, uniform and large area films are readily achievable, resulting in high quality and reproducible thin-films [12-14]. This fact has brought, therefore, many attempts to apply the vacuum process to the fabrication of perovskite films. After the first report on vacuum co-deposited halide perovskite for solar cell application by *M. Liu* et al., in 2013, numerous groups reported on vacuum-deposited perovskite solar cells[15-42]. In spite of these achievements, the sublimation of the organic ammonium halide salts remains a critical factor in achieving reproducible results. This has

been most widely described for one of the archetype precursor, CH_3NH_3I, (methylammonium iodide, MAI). Numerous groups reporting vacuum processed perovskites have described the complications of controlling the sublimation of MAI [17-21, 27, 30, 31, 38-43].

One of the merits of vacuum processing is the control over the deposited film composition via in-situ monitoring the rate of the precursors using quartz crystal microbalances (QCMs). A QCM allows for very high accuracy in deposition as it provides a sensitivity of less than ~1 $Å \cdot s^{-1}$ in real time. Compared with other techniques that determine the perovskite film composition, this is the only one allowing for a direct control during film growth. In fact, most reports on perovskite thin films and their devices report the precursor ratios from the starting solution. It is than assumed that this precursor solution ratio is maintained in the final film. This, however, is unlikely due to the different solubilities of the precursors in the solvent used. When solvent engineering is used to prepare high quality perovskite films, the use of a second solvent further complicates the determination of the thin film composition. Post preparation methods to study the composition, are not readily available. X-ray photoelectron spectroscopy (XPS) give rather good information on the composition, but only at the surface of the film. Energy-dispersive X-ray spectroscopy (EDX) can provide bulk information but the quantification of the composition could be challenging due to the limiting factors such as complex matrix effects and beam induced damage under electron radiation [44-46]. Optical analysis of the perovskite films, allows to determine the bandgap and from that estimations on the composition have been derived. When comparing reports from different groups on the bandgaps for identical compositions (inferred from the precursor solution composition) it is clear that differences in the final film composition exist [47-53], Fig. S1.

Therefore, making use of the QCMs in vacuum sublimed perovskites would be advantageous for the direct determination of the final film composition. However, this has so far not been achieved

quantitatively, due to complications arising from the sublimation of the organic ammonium halides. These complications range from uncontrolled working pressure[18, 30, 31], to fluctuating deposition rate when maintaining the source temperature constant [17, 29, 38]. These effect might be alleviated by modifying the direction or position of QCM [22, 54], control on the chamber pressure rather than on the deposition rate[18, 27, 31] and flash-evaporations from pre-formed perovskites from a single source[55]. In addition, there have been attempts to investigate the reason why the organic ammonium halides are difficult to control during its sublimation in vacuum conditions. Thermal decomposition, uncontrollable impurities and also surface varied adsorption/electronic properties have been suggested as the origins of the unusual sublimation behavior of alkylammonium halides[39, 56-58]. Despite these difficulties, perovskite based solar cells with high PCEs were obtained using vacuum-based deposition processing of the lead and alkylammonium salts. However, the level of compositional control is still much lower compared to typical vacuum processed organic films such those used in OLEDs and organic photovoltaics (OPVs).

In this paper, we study in detail the deposition of MAI and PbI_2 as well as the resulting $MAPbI_3$ perovskite using vacuum sublimation. Using various QCMs we suggest a simple method to estimate and control the molar composition of vacuum deposited $MAPbI_3$. The MAI adsorption can be characterized as a surface dependent and diffusion driven process. We established the kinetic equations for the growth rate of MAI in vacuum, extracted from the QCM. Furthermore, considering the surface dependent adsorption of MAI and taking into account geometric factors, we show it is straightforward to estimate the composition of $MAPbI_3$ films from the experimental QCM data. Using this method of control, we demonstrate all-vacuum-processed perovskite solar cells with average PCE exceeding 18%. We believe that this work will foster the general

application of vacuum processes to the deposition of perovskite films, promoting their adoption in industrial manufacturing.

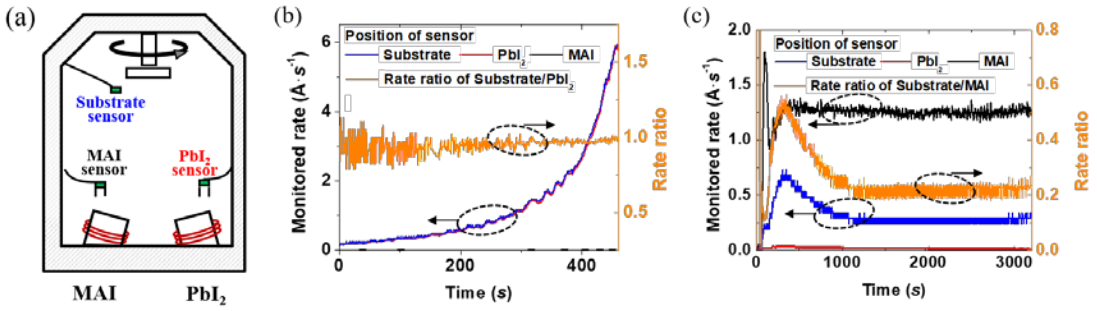

Figure 1. (a) Schematics of the experimental set up used in the deposition study. **(b)** Deposition rates and rate-ratios from different sensors when only PbI_2 is evaporated **(c)** and when only MAI is evaporated. (In the time *x*-axis, the zero is defined as the moment when the deposition rates becomes positive, after pre-heating.)

Fig. 1a shows the experimental set-up used for the deposition study. It includes two temperature controlled evaporation sources, used for MAI and PbI_2, respectively, with their corresponding QCM thickness sensors: MAI sensor (*S-MAI*), PbI_2 sensor (*S-PbI₂*) . These are positioned such that the third sensor close to the substrate (*S-Sub*) detects both MAI and PbI_2, whereas the two QCMs close to the MAI and PbI_2 sources primarily detect sublimed material from either one of them (*S-MAI* only detects MAI, whereas *S-PbI₂* only detects PbI_2). As the geometrical arrangement of the QCM sensors is different, their respective tooling factors were determined. When only PbI_2 is evaporated, the deposition rates from *S-Sub* and *S-PbI₂* display identical values as demonstrated in Fig. 1b and Fig. S2. During the evaporation of PbI_2, as shown in Fig. 1b, there is no cross-reading on the *S-MAI*. Fig. 1c displays the deposition rates when only MAI is evaporated. As described above, the MAI evaporation is challenging in part due to the cross-reading at unintended sensors. To alleviate this problem, we used a small shield around the QCM, as indicated in Fig. 1a

(Fig. S3), which resulted in negligible cross-reading during the sublimation of MAI on *S-PbI₂* (see red curve in Fig. 1c). Upon heating the MAI source, the monitored deposition rates from both *S-MAI* and *S-Sub* simultaneously increase and after a short time, the MAI rates become constant on both *S-MAI* and *S-Sub*. This behavior, an initial transient region with fluctuating rates followed by a stabilized region is observed repeatedly for different batches of MAI (see Fig. S4). The deposition rate fluctuations in the transient region are slightly differed from batch to batch, however, for all batches of MAI the rates become constant. Here, the tooling factor determined for *S-Sub* is maintained same from Fig. 1b, to display identical value with *S-PbI₂* from PbI_2 source, hence the rates at *S-Sub* and *S-MAI* are different.

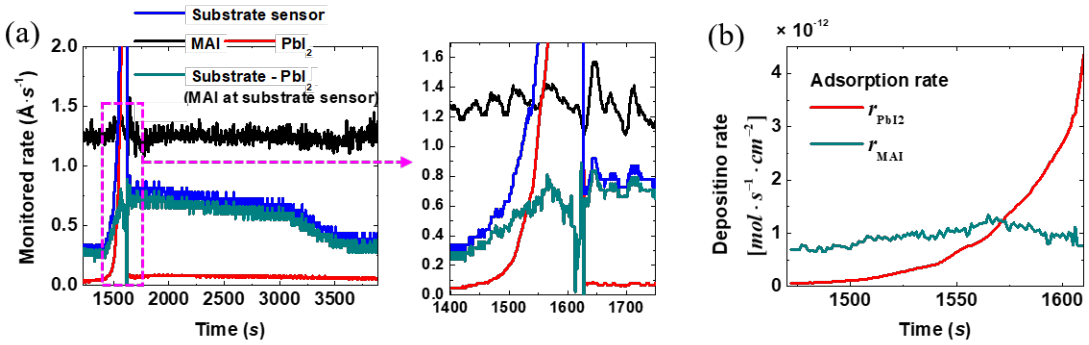

Figure 2. (a) Monitored deposition rates from the sensors with increased PbI_2 rates under constant MAI rate (left) and magnified image (right). **(b)** Adsorption of MAI and PbI_2 converted to the unit of $mol \cdot s^{-1} \cdot cm^{-2}$ from in Fig. 2a.

Fig. 2a shows the deposition rate change from *S-Sub* with increasing the PbI_2 rate during the constant MAI rate regime. We recall that the contribution of the PbI_2 deposition rates read by *S-Sub* and *S-PbI₂* are equivalent, whereas the rate measured by *S-Sub* corresponds to the sum of both MAI and PbI_2. Before the PbI_2 evaporation, the MAI rate was maintained at ~0.3 Å·s^{-1} at *S-Sub*, and upon the evaporation of PbI_2 the *S-sub* reading increased progressively with increasing PbI_2 rates. As we established that the PbI_2 rate on *S-Sub* and *S-PbI₂* have a linear correlation, we can

deduce the effective MAI rate on *S-Sub* by subtracting the PbI_2 rate from the total. Interestingly, we find that the effective MAI deposition rate increases with increasing PbI_2 rate and reaches a maximum *S-Sub* reading around 0.8 Å·s^{-1} , at a PbI_2 rate of ~1.6 Å·s^{-1} . Therefore, in the presence of PbI_2 the adhesion of MAI is increased to a maximum of 2.7 times compared to MAI alone. Further increase of the PbI_2 rate, up to 13 Å·s^{-1} as shown in Fig. S5, resulted in the decrease of the MAI rate at *S-Sub* to ~0.4 Å·s^{-1} . When, after the PbI_2 deposition at such high rates, we suddenly reduce this to zero by closing the shutter above the PbI_2 crucible, the MAI rate increases again to its former maximum value of ~ 0.8 Å·s^{-1} . With longer sublimation of MAI only, its corresponding rate from *S-Sub* gradually decreased to a value of 0.3 Å·s^{-1} , which is the same deposition rate as before the PbI_2 evaporation. This rather slow decrease of the MAI rate upon ceasing to evaporate PbI_2 is due to the fast diffusion of MAI into the PbI_2. In order to allow for a quantitative analysis, the adsorption rates of MAI (r_{MAI}) and PbI_2 (r_{PbI_2}) are expressed in the unit of $mol \cdot s^{-1} \cdot cm^{-2}$. The adsorbed mass is related to the frequency change of the QCM (Δf) according to the Sauerbrey equation[59],

$$\Delta f = -c \cdot \Delta m \qquad (1)$$

The monitored thickness can be readily converted to the frequency change of the QCM, using the data provided by the manufacturer of the crystal sensors: in our case 1 Å corresponds to $\Delta f = -0.842$ Hz . Where c is the sensitivity factor for the crystal (0.081 $Hz \cdot ng^{-1} \cdot cm^{-2}$ for 6 Mhz crystal) and Δm the adsorbed mass change. Therefore, dividing Δm by the molar mass will give the number of adsorbed molecules per time unit, which is the same as the rate of the adsorbed molecules. As displayed in Fig. 2b, r_{MAI} is maximum when it is similar to r_{PbI_2} . Upon a further increase of r_{PbI_2} , r_{MAI} decreases. This implies that the adsorption of MAI is highest on the

stoichiometric perovskite surface, and with increasing r_{PbI_2} the surface on the crystal is converted into a PbI_2 rich perovskite phase on which the MAI adsorption rate is decreased.

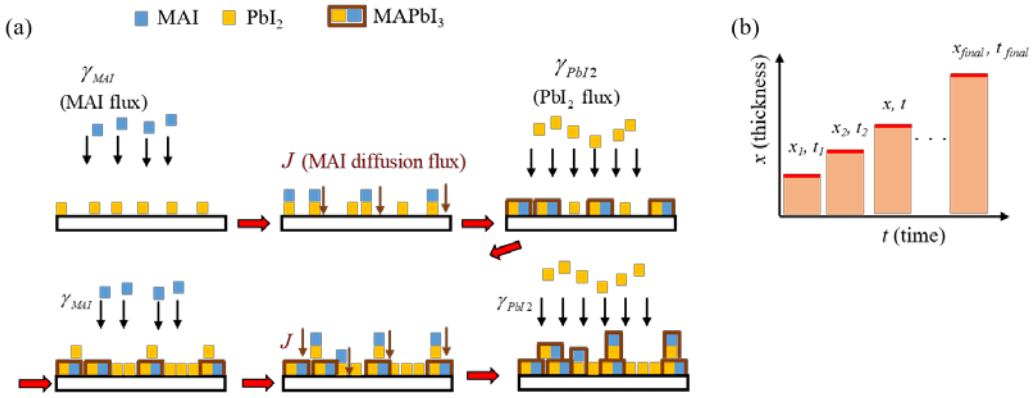

Figure 3. (a) Schematic illustration of the main processes governing the co-deposition of MAI and PbI_2 in vacuum deposition and **(b)** the resultant thickness of the grown perovskite film as a function of *x* and *t*.

To facilitate a more in depth discussion of the co-deposition process as monitored in Fig. 2, it is useful to assume that the MAI and PbI_2 alternatively come into contact with the surface. This simplification allows us to describe the different steps involved in the adsorption of the MAI and PbI_2 and its subsequent conversion into the perovskite. As we have shown that the adsorption of MAI on the bare QCM is not favored, we can reasonably assume that the first step is the deposition of PbI_2 (depicted as the yellow blocks in Fig. 3a). As in our approximation the two materials hit the substrate in an alternating manner, the subsequent step is the adsorption of MAI. The MAI primarily adheres on the PbI_2 covered areas (as the adsorption on PbI_2 is much more efficient than on the bare QCM surface), however, the deposition of MAI on PbI_2 leads to the formation of the perovskite which depends on the diffusion of MAI into the PbI_2 and/or partially formed $MAPbI_3$ perovskite (schematically shown in Fig. 3a as the brown line around the yellow and blue PbI_2 and

MAI blocks). In this assumption, during the co-deposition of MAI and PbI_2 there are 3 different surfaces, PbI_2, MAI and the resulting $MAPbI_3$ perovskite. To establish the growth kinetics, we can start from the general equation for the adsorption rate as follows.

$$r_{ads.} = \varphi S \quad (2)$$

where φ is the impingement rate which is the number of molecules striking the surface per unit time and area, and S is the sticking probability, $S = \sigma \exp\{-E_{act} / k_B T\} f(\theta)$. ($\sigma$: condensation coefficient, E_{act}: activation energy for adsorption, k_B: Boltzman constant, T: temperature, $f(\theta)$: surface coverage function for probability of finding an adsorption site)[60]. In the case of the sticking of MAI on PbI_2, the perovskite is formed by the chemical reaction. Hence, this sticking can be characterized as the chemisorption, where the E_{act} would also related to the activation energy for the chemical reaction. Regarding the surfaces, as mentioned earlier, the MAI adsorption rates is surface dependent, thus it can be expressed considering the 3 different surfaces separately. Modifying eqn (2) then,

$$r_{MAI} = \varphi_{MAI} \left\{ \sum_i S_i f(\theta_i) \right\} = \varphi_{MAI} \left\{ S_{MAI} f(\theta_{MAI}) + S_{PbI_2} f(\theta_{PbI_2}) + S_{perov.} f(\theta_{perov.}) \right\} \quad (3)$$

Where S_i refers to the intrinsic sticking coefficient (or $\sigma \exp\{-E_{act} / k_B T\}$) of MAI on a surface of the different materials i (e.g., i = MAI, PbI_2 and $MAPbI_3$), and $f(\theta_i)$ is defined as the fractional ratio of coverage by the species i. For example, θ_{MAI} is the surface area covered by MAI/total surface area ($\sum_i \theta_i = 1$). The surface area for the different compounds can be assumed to be proportional to their respective adsorption rate and their molar mass divided by their density, as described below,

$$\text{Area covered by } i \text{ under deposition, } \theta_i, \propto \frac{M_i}{\rho_i} r_i \qquad (4)$$

Where M_i and ρ_i are the molar mass and density of *i*, respectively. During co-sublimation of both MAI and PbI_2, the diffusion flux of MAI, *J*, should also be taken into account to correctly determine the coverage. This is needed as upon the diffusion of MAI into PbI_2 the perovskite is formed, eliminating MAI and PbI_2 from the surface (Fig. 3a), where the *J* can be represented as a function of *x* and *t* as shown in Fig. 3b, with respect to the concentration gradient of MAI from surface. When taking all these factors into account we can consider two regimes during the sublimation: either $r_{PbI_2} < r_{MAI}$ or $r_{MAI} < r_{PbI_2}$ and for both cases we can derive a dependency on each other as depicted in Fig. 4 (The derivation is described in detail in the Supporting information).

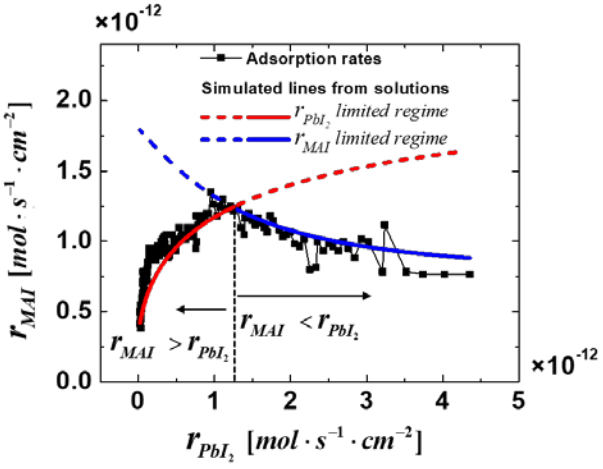

Figure 4. PbI_2 rate *vs* MAI rate extracted from Fig. 2b with simulated lines using the derived growth equations for the either the r_{MAI} or r_{PbI_2} dominant rate regimes. (The equations are described in the Supporting information.)

The experimental data points are in good agreement with the fitting curves from the derived equations. The values of $\varphi_{MAI} = 1.4 \times 10^{-12}\ mol \cdot s^{-1} \cdot cm^{-2}$, $S_{PbI_2} = 0.50$ and $S_{MAI} = 0.23$ used for the

numerical fitting are physically meaningful. The impingement rate φ_{MAI}, 1.4×10^{-12} $mol\cdot s^{-1}\cdot cm^{-2}$, is always higher than r_{MAI}. The sticking probability is also similar to the value extracted by another simple definition of the probability which is,

$$\text{Sticking probability} = \frac{\#\text{ of adsorbed molecule}}{\#\text{ of striking molecule}} = \frac{r_{MAI}}{\varphi_{MAI}} \qquad (5)$$

For example, when r_{PbI_2}=0, the surface of the film will be full of MAI under the constant φ_{MAI}, hence we can estimate the S_{MAI} using eqn (5), with corresponding values of φ_{MAI} and r_{MAI}. As shown in Fig. 4, the r_{MAI} = 0.38×10^{-12} $mol\cdot s^{-1}\cdot cm^{-2}$ results in S_{MAI} = 0.27, which is close to the result, S_{MAI} = 0.23, previously calculated by the proposed solutions. S_{PbI_2} can be estimated in the same manner assuming that adsorption of MAI on PbI_2 would be dominant in the region where the r_{PbI_2} is much faster than r_{MAI}. As shown in Fig. 4, when r_{PbI_2} reaches the highest value, over 4×10^{-12} $mol\cdot s^{-1}\cdot cm^{-2}$, r_{MAI} approaches ~0.8×10^{-12} $mol\cdot s^{-1}\cdot cm^{-2}$, resulting in the S_{PbI_2} = 0.57 from the definition in eqn (5), which is also similar to the calculated result from the solutions, 0.50. Therefore, our suggested growth model accurately describes the vacuum deposition process for $MAPbI_3$ perovskites.

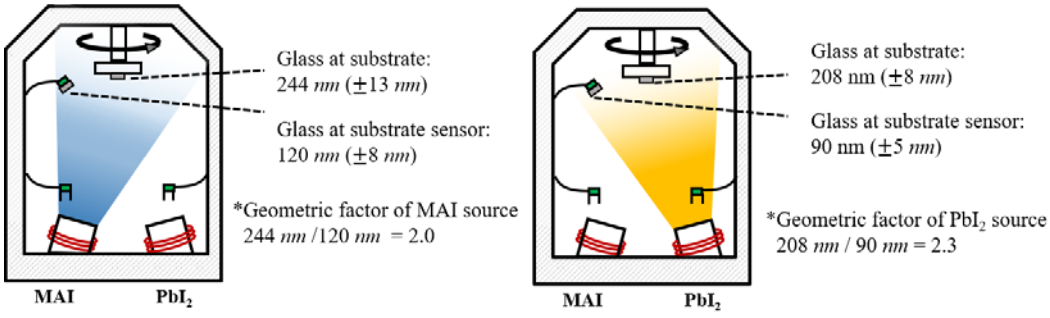

Figure 5. Schematic figure for calibration of the geometric factor, $\frac{Thickness\ at\ substrate}{Thickness\ at\ sub.sensor}$, for MAI and PbI_2.

Considering the enhanced adsorption of MAI with PbI_2, it is possible to estimate and control the composition of the perovskite film in vacuum co-deposition using the evaporation system described in Fig. 1a, as well as in Fig. 5. Since the *S-Sub* reads both MAI and PbI_2, therefore, the enhanced adsorption of MAI on PbI_2 is already taken into account at the *S-Sub*. In addition, the adsorbed thickness ratio on the *S-Sub* will be directly proportional to the adsorbed mass ratio, which can be simply calculated by dividing their molar mass even without considering the Sauerbrey equation. However, one should be aware that *S-Sub* is off-centered to prevent the shadows on the substrate by evaporated materials from the crucible sources. This results in different amount of molecules reaching the *S-Sub* and the substrate, depending on the location of the crucibles. To calibrate this difference caused by the geometrical factor, we positioned two glass substrates; one is at the normal substrate holder and another is at the sensor by attaching it to the sensor head as illustrated in Fig. 5. Afterwards, MAI and PbI_2 are separately evaporated and the thickness of the evaporated films on the glass substrates is measured as demonstrated in Fig. 5. In our case, the ratio of $\frac{Thickness\ at\ substrate}{Thickness\ at\ sub.sensor}$ is 2.0 and 2.3 for the MAI and PbI_2 sources respectively. In this correction, we assumed that during the perovskite co-deposition, the different sub-layers (e.g. glass, Au-coated QCM, and organic charge transporting layer) have a negligible effect on the overall adsorption rate of the perovskite. The different sub-layers will affect the initial growth rate for the perovskite, however, once the surface is fully covered by the deposited perovskite, the surface dependent growth property can be excluded. From the work of Olthof and Meerholz it is known that after approximately 10 nm of deposition the surface is completely covered with a perovskite film[58]. In view of the final perovskite film thickness we deposit, (usually over 500 nm for active layer), we can assume that the surface effect is negligible for the growth rate of the thick perovskite.

It is important to note that the consideration of the geometric factor enables us to directly control the composition of the perovskite by monitoring the actually adsorbed precursor amount. This is an important advantage of vacuum deposition as other processes use indirect methods to estimate the composition. These range from XPS, EDX or even by assuming complete deposition of the precursors from solution. In that method the composition of the film is usually estimated by weighing the precursors, which may result in large errors due to the different solubility and coating yields of the precursors [61, 62].

Table 1. Monitored thicknesses and calculated molar ratios of co-evaporated perovskite film under 4 different conditions

	Film 1	**Film 2**	**Film 3**	**Film 4**
Monitored thickness at *substrate sensor* [PbI_2 / MAI] (nm)	430 / 104	441 / 145	440 / 183	410 / 237
Weight ratio of [PbI_2:MAI] at *substrate sensor*	1 : 0.24	1 : 0.34	1 : 0.42	1 : 0.58
Calculated molar ratio of PbI_2:MAI at *substrate*	1 : 0.61	1: 0.85	1 : 0.95	1 : 1.45

(* The thickness of MAI is nominal value, where the same tooling factor was used with PbI_2. *The molar ratio at substrate calculated from weight ratio divided by molar masses and multiplied by geometric factor, defined as $\frac{Thickness\ at\ substrate}{Thickness\ at\ sub.Sensor}$)

Based on this method, we fabricated four different perovskite films with a fixed PbI_2 rate of 1 Å·s^{-1} , and varying MAI rates as monitored by *S-Sub.* Again, since the PbI_2 rate on *S-Sub* and *S-PbI_2* have a linear correlation, it is able to monitor and control the adsorbed MAI rate on *S-Sub* by subtracting the PbI_2 rate from the total on *S-Sub*. The resulting final thicknesses as deduced from *S-Sub* for PbI_2 and MAI are shown in Table 1. Using the previously-described methodology, the composition of the co-evaporated films at the substrate was calculated. Film 3 is close to the 1:1 stoichiometry for PbI_2:MAI. The measured thickness and absorbance of the films are in Fig. S6.

We used these films to prepare thin film solar cells in the *p-i-n* configuration according to the schematic drawing depicted in Fig.6a. We used an all vacuum process as reported previously [63].

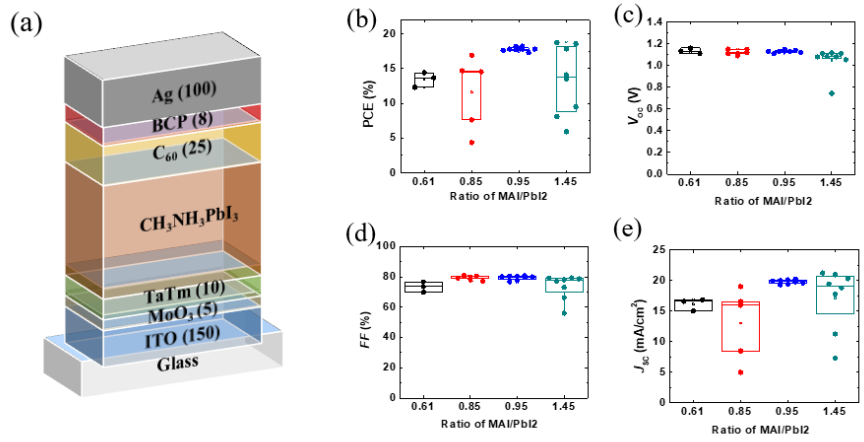

Figure 6. (a) Structure of the fabricated device **(b-e)** Statistics of the photovoltaic parameters

The solar cells based on film 1 and 2 did not lead to very high power conversion efficiencies (PCEs) (Fig. 6b). Those based on film 3 and 4 performed much better, although the devices using film 4 showed a larger spreading in particular of the short circuit current density (J_{SC}). The best performance in absolute PCE and spreading were obtained for the solar cells employing film 3. That is, the perovskite film with an almost stoichiometric composition. Since it is known that the best performance is obtained for perovskite films that are close to the ideal stoichiometry, this finding further corroborates that the method we developed indeed allows to determine the perovskite composition. The origin of wide distribution in J_{SC} and *FF* in MAI deficient and in particular the PbI_2 deficient films is not clear but it is speculated that it can be caused by unstable perovskite active layer originating from non-stoichiometry.

In conclusion, we established the growth kinetics of $MAPbI_3$ in a vacuum based sublimation process. For this, we positioned the source QCMs in such a way that they selective monitor only

one precursor sublimation rate. To monitor the co-deposition of both precursors, a third sensor close to the substrate is used. By careful studying the rates on each of these QCMs in different sublimation conditions, we have developed a simple model describing the growth kinetics. Using this model we are able to control the molar composition of the $MAPbI_3$ in vacuum co-deposition process. This is an important step forward as now direct control over the final film composition is available whereas previously this had to be obtained off line after film deposition. As mentioned, in-situ composition control is extensively used in other vacuum-based processing methods, such as OLEDs and we believe this will provide meaningful insights for general application of the vacuum process for the fabrication of perovskites films.

Acknowledgements

The research leading to these results has received funding from European Union's Horizon 2020 research and innovation programme under grant agreement No. 763977 of the PERTPV project, the Spanish Ministry of Science, Innovation and Universities (MINECO), MAT2017-88821-R, RTI2018-095362-A-I00, PCI2019-111829-2 and CEX2019-000919-M and the Comunitat Valenciana IDIFEDER/2018/061. M.S. acknowledges the MINECO for his RyC.

References

[1] Kojima, A.; Teshima, K.; Shirai, Y.; Miyasaka, T. Organometal Halide Perovskites as Visible-Light Sensitizers for Photovoltaic Cells. *J. Am. Chem. Soc*. **2009**, 131, 6050–6051.

[2] J. H. Im, C. R. Lee, J. W. Lee, S. W. Park, N. G. Park , 6.5% Efficient Perovskite Quantum-Dot-Sensitized Solar Cell. *Nanoscale* 3, **2011,** 4088.

[3] NREL https://www.nrel.gov/pv/cell-efficiency.html,

[4] Burschka, J.; Pellet, N.; Moon, S. J.; Humphry-Baker, R.; Gao, P.; Nazeeruddin, M. K.; Gratzel, M. Sequential Deposition as a Route to High-Performance Perovskite-Sensitized Solar Cells. *Nature* **2013**, 499, 316–319.

[5] Yang, W. S.; Park, B.-W.; Jung, E. H.; Jeon, N. J.; Kim, Y. C.; Lee, D. U.; Shin, S. S.; Seo, J.; Kim, E. K.; Noh, J. H.; et al. Iodide Management in Formamidinium-Lead-Halide−based Perovskite Layers for Efficient Solar Cells. *Science* **2017**, 356, 1376−LP-1379.

[6] Jeon, N. J.; Noh, J. H.; Kim, Y. C.; Yang, W. S.; Ryu, S.; Seok, S. Solvent Engineering for High-Performance Inorganic–Organic Hybrid Perovskite Solar Cells. *Nat. Mater.* **2014,** *13*,897–903.

[7] Chen, Q.; Zhou, H.; Hong, Z.; Luo, S.; Duan, H.-S.; Wang, H.-H.; Liu, Y.; Li, G.; Yang, Y. Planar Heterojunction Perovskite Solar Cells via Vapor-Assisted Solution Process. *J. Am. Chem. Soc.* **2014,** *136*, 622–625.

[8] Leyden, M. R.; Ono, L. K.; Raga, S. R.; Kato, Y.; Wang, S. H.; Qi, Y. B. High Performance Perovskite Solar Cells by Hybrid Chemical Vapor Deposition. *J. Mater. Chem. A* **2014**, 2, 18742−18745.

[9] Peng, Y.; Jing, G.; Cui, T. A Hybrid Physical–Chemical Deposition Process at Ultra-Low Temperatures for High-Performance Perovskite Solar Cells. *J. Mater. Chem. A* **2015**, 3, 12436-12442.

[10] Li, Y.; Cooper, J. K.; Buonsanti, R.; Giannini, C.; Liu, Y.; Toma, F. M.; Sharp, I. D. Fabrication of Planar Heterojunction Perovskite Solar Cells by Controlled Low-Pressure Vapor Annealing. *J. Phys. Chem. Lett.* **2015**, 6, 493−499.

[11] Dunlap-Shohl, W. A.; Zhou, Y.; Padture, N. P.; Mitzi, D. B. Synthetic Approaches for Halide Perovskite Thin Films. *Chem. Rev.* **2019**, 119, 3193−3295.

[12] Ávila, J.; Momblona, C.; Boix, P. P.; Sessolo, M.; Bolink, H. J. Vapor-Deposited Perovskites: The Route to High-Performance Solar Cell Production?. *Joule* **2017** 1, 431– 442.

[13] Shen, P.-S.; Chiang, Y.-H.; Li, M.-H.; Guo, T.-F.; Chen, P. Research Update: Hybrid Organic-Inorganic Perovskite (HOIP) Thin Films and Solar Cells by Vapor Phase Reaction. *APL Mater*. **2016**, 4, 091509.

[14] Kim, H.; Lim, K.-G.; Lee, T.-W. Planar Heterojunction Organometal Halide Perovskite Solar Cells: Roles of Interfacial Layers. *Energy Environ. Sci*., **2016,** 9, 12-30.

[15] Ono, L. K.; Leyden, M. R.; Wang, S.; Qi, Y.; Organometal Halide Perovskite Thin Films and Solar Cells by Vapor Deposition. *J. Mater. Chem. A*, **2016,** 4, 6693-6713.

[16] Liu, M.; Johnston, M. B.; Snaith, H. J. Efficient Planar Heterojunction Perovskite Solar Cells by Vapour Deposition. *Nature* **2013,** *501*, 395–398.

[17] Malinkiewicz, O.; Yella, A.; Lee, Y. H.; Espallargas, G. M.; Graetzel, M.; Nazeeruddin, M. K.; Bolink, H. J. Perovskite Solar Cells Employing Organic Charge-Transport Layers. *Nat. Photonics* **2013,** *8*, 128–132.

[18] Polander, L.E.; Pahner, P.; Schwarze, M.; Saalfrank, M.; Koerner, C.; Leo, K. Hole-Transport Material Variation in Fully Vacuum Deposited Perovskite Solar Cells. *APL Mater.* **2014,** *2*, 081503.

[19] Kim, B.-S.; Kim, T.-M.; Choi, M.-S.; Shim, H.-S.; Kim, J.-J. Fully Vacuum–Processed Perovskite Solar Cells with High Open Circuit Voltage Using MoO_3/NPB as Hole Extraction Layers. *Organic Electronics* **2015,** *17*, 102–106.

[20] Lin, Q.; Armin, A.; Nagiri, R. C. R.; Burn, P. L.; Meredith, P. Electro-optics of perovskite solar cells. *Nat. Photonics* **2014,** 9, 106−112.

[21] Ng, T.-W.; Chan, C.-Y.; Lo, M.-F.; Guan, Z. Q.; Lee, C.-S. Smooth Perovskite Thin Films and Efficient Perovskite Solar Cells Prepared by the Hybrid Deposition Method. *J. Mater. Chem. A* **2015,** 3, 9081– 9085.

[22] Ono, L. K.; Wang, S.; Kato, Y.; Raga, S. R.; Qi, Y. Fabrication of Semi-transparent Perovskite Films with Centimeter-scale Superior Uniformity by the Hybrid Deposition Method. *Energy Environ. Sci*. **2014**, 7, 3989– 3993.

[23] Subbiah, A. S.; Halder, A.; Ghosh, S.; Mahuli, N.; Hodes, G.;Sarkar, S. K. Inorganic Hole Conducting Layers for Perovskite-Based Solar Cells *J. Phys. Chem. Lett*. **2014,** 5, 1748−1753.

[24] Gao, C.; Liu, J.; Liao, C.; Ye, Q.; Zhang, Y.; He, X.; Guo, X.; Mei, J.; Lau, W. Formation of Organic–Inorganic Mixed Halide Perovskite Films by Thermal Evaporation of $PbCl_2$ and CH_3NH_3I Compounds. *RSC Adv*., **2015,** 5, 26175.

[25] Tran, D. T. C.; Liu, Y.; Thibau, E. S.; Llanos, A.; Lu, Z.-H. Stability of Organometal Perovskites with Organic Overlayers. *AIP ADVANCES* **2015,** 5, 087185.

[26] Borchert, J.; Boht, H.; Fränzel, W.; Csuk, R.; Scheer, R.; Pistor, P. Structural Investigation of Co-Evaporated Methyl Ammonium Lead Halide Perovskite Films during Growth and Thermal Decomposition Using Different PbX_2 (X = I, Cl) Precursors. *J. Mater. Chem. A*, **2015,** 3. 19842.

[27] Teuscher, J.; Ulianov, A.; Müntener, O.; Grätzel, M.; Tetreault, N. Control and Study of the Stoichiometry in Evaporated Perovskite Solar Cells. *ChemSusChem* **2015,** 8, 3847−3852.

[28] Su, Z.; Hou, F.; Jin, F.; Wang, L.; Li, Y.; Zhu, J.; Chu, B.; Li, W. Hole Transporting Material-Free and Annealing-Free Thermal Evaporated Planar Perovskite Solar Cells with an Ultra-Thin $CH_3NH_3PbI_{3-X}Cl_X$ layer. *Organic Electronics* **2015,** 26, 104-108.

[29] Ke, W.; Zhao, D.; Grice, C.R.; Cimaroli, A.J.; Fang, G.; Yan, Y. Efficient Fully-Vacuum-Processed Perovskite Solar Cells Using Copper Phthalocyanine as Hole Selective Layers *J. Mater. Chem. A*, **2015,** 3, 23888-23894.

[30] Momblona, C.; Gil-Escrig, L.; Bandiello, E.; Hutter, E.M.; Sessolo, M.; Lederer, K.; Blochwitz-Nimoth, J.; Bolink, H. J. Efficient Vacuum Deposited p-i-n and n-i-p Perovskite Solar Cells Employing Doped Charge Transport Layers. *Energy Environ. Sci.* **2016,** ,9, 3456-3463.

[31] Kim, B.-S; Choi, M.-H.; Choi, M.-S.; Kim, J.-J.; Composition-Controlled Organometal Halide Perovskite via CH_3NH_3I Pressure in a Vacuum Co-Deposition Process. *J. Mater. Chem. A*, **2016,** 4, 5663-5668.

[32] Zou, Y.; Meng, Q.; Mao, H. Y.; Zhu, D. B. Substrate Effect on the Interfacial Electronic Structure of Thermally-Evaporated $CH_3NH_3PbI_3$ Perovskite Layer. *Org. Electron.* **2017,** 41, 307– 314.

[33] Zhao, D.; Ke, W.; Grice, C. R.; Cimaroli, A. J.; Tan, X.; Yang, M.; Collins, R. W.; Zhang, H.; Zhu, K.; Yan, Y. Annealing-Free Efficient Vacuum-Deposited Planar Perovskite Solar Cells with Evaporated Fullerenes as Electron-Selective Layers. *Nano Energy* **2016,** 19, 88−97.

[34] Calio, L.; Momblona, C.; Gil-Escrig, L.; Kazim, S.; Sessolo, M.;́Sastre-Santos, Á .; Bolink, H. J.; Shahzada, A. Vacuum Deposited Perovskite Solar Cells Employing Dopant-Free Triazatruxene as the Hole Transport Material. Sol. Energy Mater. Sol. Cells 2017, 163, 237−241.

[35] Song, H.-J.; Lee, H.; Ahn, S.; Song, H.; Lee, C. Perovskite Photovoltaic Cells with Ultra-Thin Buffer Layers for Tandem Application. *Jpn. J. Appl. Phys*. **2018,** 57, 102303.

[36] Arivazhagan, V.; Xie, J.; Yang, Z.; Hang, P.; Parvathi, M. M.; Xiao, K,; Cui, C.; Yang, D.; Yu, X.; Vacuum co-deposited $CH_3NH_3PbI_3$ Films by Controlling Vapor Pressure for Efficient Planar Perovskite Solar Cells. *Solar Energy*, **2019**, 181, 339-344

[37] Xu, H.; Xu, F.; Wang, W.; Zhu, Y.; Fang, Z.; Yao, B.; Hong, F.; Cui, J.; Xu, F.; Xu, R.; Chen, C.-C. Wang, L.; Resolving the Detrimental Interface in Co-Evaporated $MAPbI_3$ Perovskite Solar Cells by Hybrid Growth Method. *Organic Electronics* **2019** 69, 329-335.

[38] Li, J.; Wang, H.; Chin, X. Y.; Dewi, A. H.; Vergeer, K.; Goh, T. W.; Lim, J. W. M.; Lew, J. H.; Loh , K. P.; Soci, C.; et al. Highly Efficient Thermally Co-evaporated Perovskite Solar Cells and Mini-module. *Joule*, **2020**, 4, 1035–1053.

[39] Emara, J.; Schnier, T.; Pourdavoud, N.; Riedl, T.; Meerholz, K.; Olthof, S. Impact of Film Stoichiometry on the Ionization Energy and Electronic Structure of $CH_3NH_3PbI_3$ Perovskites. *Adv. Mater*. **2016**, 28, 553– 559.

[40] Chen, C. W.; Kang, H. W.; Hsiao, S. Y.; Yang, P. F.; Chiang, K. M.; Lin, H. W. Efficient and Uniform Planar-Type Perovskite Solar Cells by Simple Sequential Vacuum Deposition. *Adv. Mater*. **2014,** 26, 6647−6652.

[41] D. Yang, Z. Yang, W. Qin, Y. Zhang, S,. Liu, C. Li. Alternating Precursor Layer Deposition for Highly Stable Perovskite Films Towards Efficient Solar Cells using Vacuum Deposition. *J. Mater. Chem. A* **2015,** 3, 9401.

[42] Hsiao, S.-Y.; Lin, H.-L.; Lee, W.-H.; Tsai, W.-L.; Chiang, K-M.; Liao, W.-Y.; Ren-Wu, C.-Z.; Chen, C.-Y.; Lin, H.-W. Efficient All-Vacuum Deposited Perovskite Solar Cells by Controlling Reagent Partial Pressure in High Vacuum. *Adv. Mater.* **2016**, 28, 7013-7019.

[43] Wang, S.; Ono, L. K.; Leyden, M. R.; Kato, Y.; Raga, S. R.; Lee, M. V.; Qi, Y. Smooth Perovskite Thin Films and Efficient Perovskite Solar Cells Prepared by the Hybrid Deposition Method. *J. Mater. Chem. A* **2015,** 3, 14631−14641.

[44] Jany, B. R.; Janas, A.; Krok, F. Retrieving the Quantitative Chemical Information at Nanoscale from Scanning Electron Microscope Energy Dispersive X-Ray Measurements by Machine Learning. Nano Lett. 2017, 17, 6520– 6525.

[45] Newbury, D. E.; Ritchie, N. W. M. Is Scanning Electron Microscopy/Energy Dispersive X-ray Spectrometry (SEM/EDS) Quantitative? *Scanning* **2013**, 35, 141–168.

[46] Rothmann, M. U.; Li, W.; Zhu, Y.; Liu, A.; Ku, Z.; Bach, U.; Etheridge, J.; Cheng, Y.-B. Structural and Chemical Changes to $CH_3NH_3PbI_3$ Induced by Electron and Gallium Ion Beams. *Adv. Mater.* **2018**, 30, 1800629

[47] Stolterfoht, M.; Wolff, C. M.; Amir, Y.; Paulke, A.; Perdigon-Toro, L. P.; Caprioglio, P.; Neher, D. Approaching the Fill Factor Shockley Queisser Limit in Stable, Dopant-Free Triple Cation Perovskite Solar Cells. *Energy Environ. Sci*. **2017**, 10, 1530–1539.

[48] Saliba, M.; Matsui, T.; Seo, J.-Y.; Domanski, K.; Correa-Baena, J.-P.; Mohammad, K. N.; Zakeeruddin, S. M.; Tress, W.; Abate, A.; Hagfeldt, A.; et all. Cesium-Containing Triple Cation Perovskite Solar Cells: Improved Stability, Reproducibility and High Efficiency. *Energy Environ. Sci*. **2016**, 9, 1989-1997.

[49] Koh, T. M.; Shanmugam, V.; Schlipf, J.; Oesinghaus, L.; Müller-Buschbaum, P.; Ramakrishnan, N.; Swamy, V.; Mathews, N.; Boix, P. P.; Mhaisalkar, S. G. Nanostructuring Mixed-Dimensional Perovskites: A Route Toward Tunable, Efficient Photovoltaics. *Adv. Mater.* **2016**, 28, 3653– 3661.

[50] Chen, P.; Bai, Y.; Wang, S.; Lyu, M.; Yun, J.; Wang, L. In Situ Growth of 2D Perovskite Capping Layer for Stable and Efficient Perovskite Solar Cells. *Adv. Funct. Mater*. **2018,** 28, 1706923.

[51] Chen, S.; Wen, X.; Yun, Jae S.; Huang, S.; Green, M.; Jeon, N. J.; Yang, W. S.; Noh, J. H.; Seo, J.; Seok, S. I.; Ho-Baillie, A. Spatial Distribution of Lead Iodide and Local Passivation on Organo-Lead Halide Perovskite. *ACS Appl. Mater. Interfaces* **2017**, 9, 6072– 6078.

[52] Zheng, F.; Wen, X.; Bu, T.; Chen, S.; Yang, J.; Chen, W.; Huang, F.; Cheng, Y.-B.; Jia, B. Slow Response of Carrier Dynamics in Perovskite Interface upon Illumination. *ACS Appl. Mater. Interfaces* **2018,** 10, 31452.

[53] Gong, X.; Sun, Q.; Liu, S.; Liao, P.; Shen, Y.; Gratzel, C.; Zakeeruddin, S. M.; Grätzel, M.; Wang, M. Highly Efficient Perovskite Solar Cells with Gradient Bilayer Electron Transport Materials. *Nano Lett*. **2018,** 18, 3969– 3977.

[54] Lohmann, K. B.; Patel, J. B.; Rothmann, M. U.; Xia, C. Q.; Oliver, R. D. J.; Herz, L. M.; Snaith, H. J.; Johnston, M. B.; Control over Crystal Size in Vapor Deposited Metal-Halide Perovskite Films. *ACS Energy Lett.* **2020**, 5(3), 710–717.

[55] Longo, G.; Gil-Escrig, L.; Degen, M. J.; Sessolo, M.; Bolink, H. J.; Perovskite solar cells prepared by flash evaporation. *Chem. Commun*. **2015**, 51, 7376– 7378.

[56] Liu, L.; McLeod, J. A.; Wang, R.; Shen, P.; Duhm, S.; Tracking the Formation of Methylammonium Lead Triiodide Perovskite. *Appl. Phys. Lett*. **2015**, 107, 061904.

[57] Borchert, J.; Levchuk, I.; Snoek, L. C. ; Rothmann, M. U.; Haver, R.; Snaith, H. J.; Brabec, C. J.; Herz, L. M., Johnston, M. B.; Impurity Tracking Enables Enhanced Control and Reproducibility of Hybrid Perovskite Vapor Deposition. *ACS Appl. Mater. Interfaces* **2019**, 11, 32, 28851-28857.

[58] Olthof, S.; Meerholz, K. Substrate-Dependent Electronic Structure and Film Formation of MAPbI3 Perovskites. *Sci. Rep*. **2017**, 7, 40267.

[59] Sauerbrey, G.; Verwendung von Schwingquarzen zur Wägung dünner Schichten und zur Mikrowägung. *Z. Phys*.**1959**, 155, 206−222

[60] Oura K.; Katayama M.; Zotov A.V.; Lifshits V.G.; Saranin A.A.; Elementary Processes at Surfaces I. Adsorption and Desorption. In: Surface Science. Advanced Texts in Physics. *Springer, Berlin, Heidelberg.* **2003**.

[61] Niu, G.; Li, W.; Li, J.; Liang, X.; Wang, L. Enhancement of Thermal Stability for Perovskite Solar Cells through Cesium Doping. *RSC Adv*. **2017**, 7, 17473– 17479.

[62] Holliman, P. J.; Jones, E. W.; Hobbs, R. J.; Connell, A.; Furnell, L.; Anthony, R.; Kershaw, C.P. Eurig Quantitative Chemical Analysis of Perovskite Deposition Using Spin Coating. *Materials Letters: X*, **2019,** 2, 100011.

[63] Pérez-del-Rey, D.; Gil-Escrig, L.; Zanoni, K. P. S.; Dreessen, C.; Sessolo, M.; Boix, P. P.; Bolink, H. J.; Molecular Passivation of MoO_3: Band Alignment and Protection of Charge Transport Layers in Vacuum-Deposited Perovskite Solar Cells. *Chem. Mater*. **2019**, 31, 6945– 6949.

Supporting information for

Deposition Kinetics and Compositional Control of Vacuum Processed $CH_3NH_3PbI_3$ Perovskite

Beom-Soo Kim, Lidón Gil-Escrig, Michele Sessolo and Henk J. Bolink*.*

Instituto de Ciencia Molecular, Universidad de Valencia, Calle Catedrático Jose Beltrán 2, Paterna, 46980, Spain.

Email: beom.kim@uv.es, henk.bolink@uv.es

Experimental

Deposition study using QCM

For every deposition study, a new QCM (Fil-Tech, 6 Mhz) was used. The deposition rates were controlled and monitored by stored program (VAKSIS) of the evaporator. The precursor materials, MAI (Lumtec) and PbI_2 (Lumtec) were introduced in the temperature controlled evaporation sources (Creaphys) through an inert atmosphere glove box. Before evaporation MAI, the source was heated at 90 ℃ at ambient pressure for ~20 minutes for out-gassing.

Device fabrication

ITO pre-patterned substrates were cleaned following a standard procedure in which they are sequentially cleaned with soap, water, deionized water, and isopropanol in a sonication bath, followed by UV treatment for 20 min. All the solar cell layers were prepared by thermal vacuum deposition

performed in vacuum chambers evacuated to a pressure of ~10^{-6} mbar, which were integrated into a nitrogen-filled glovebox (H_2O and O_2 < 0.1 ppm). TaTm, C_{60} and BCP were sublimed in the same vacuum chamber at temperatures ranging from 100 to >300 ℃, depending on the material, and the precise evaporation rate and deposited film thickness were controlled by the QCM sensors. In general, the deposition rate for TaTm and C_{60} was 0.5 Å/s while the thinner BCP layer was evaporated at 0.2−0.3 Å/s. For the perovskite deposition, MAI and PbI_2 were co-evaporated at the same time. The MAI rate was controlled by the substrate sensor, which reads both MAI and PbI_2 rates while the PbI_2 rate is maintained constant which is monitored by the QCM sensor close to the PbI_2 source. The MoO_3 and Ag were evaporated in another vacuum chamber using aluminum boats as sources by applying currents ranging from 2.0 to 4.5 A. After TaTm deposition, the substrate was heated at 140 ℃ for 10 minutes, according to previous report, *Chem. Mater*. **2019**, 31, 17, 6945-6949.

Characterization

Absorption spectra were collected using a fiber optics based Avantes Avaspec2048 Spectrometer. Characterization of the solar cells was performed as follows, using two different methods for double check. For the first, the external quantum efficiency (EQE) was measured using the cell response at different wavelength (measured with a white light halogen lamp in combination with band-pass filters), where the solar spectrum mismatch is corrected using a calibrated Silicon reference cell (MiniSun simulator by ECN, the Netherlands). Solar cells were illuminated by the halogen lamp in combination with interference filters for the EQE and J–V measurements An estimation of the short-circuit current density (J_{SC}) understandard test conditions was calculated by convolving the EQE spectrum with the AM1.5G reference spectrum, using the premise of a linear dependence of Jsc on light intensity. *J–V* characteristics of the solar cells were recorded using a Keithley2400 SourceMeter, in a −0.2 and 1.2 V voltage range, with 0.01 V steps. Also, the *J−V* curves were measured again illuminated under a Wavelabs Sinus 70 LED solar simulator. The light intensity was calibrated before

every measurement using a calibrated Si reference diode equipped with an infrared cut-off filter (KG-3, Schott). Keithley 2612A SourceMeter was used to record in a −0.2 and 1.2 V voltage range, with 0.01 V steps and integrating the signal for 20 ms after a 10 ms delay, corresponding to a speed of about 0.3 V/s.

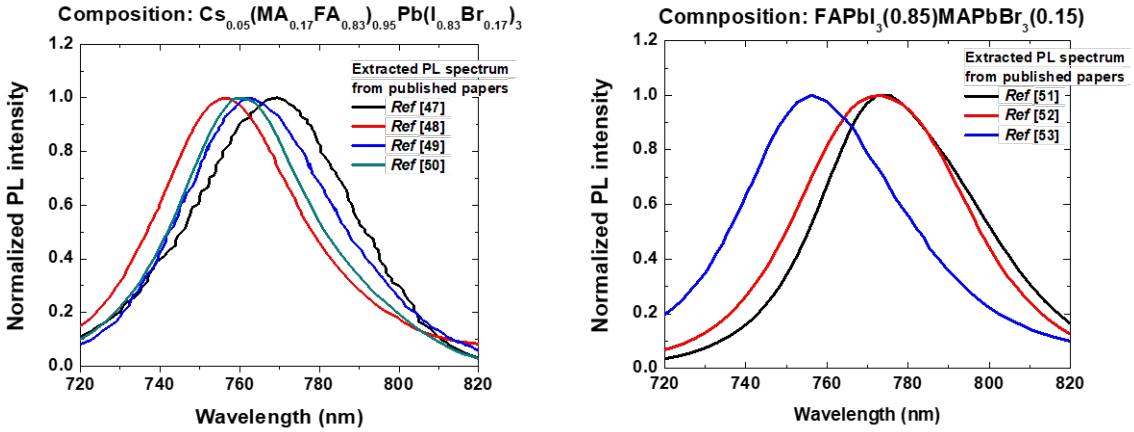

Figure S1. Extracted PL spectrum for $(Cs_{0.05}MA_{0.17}FA_{0.83})_{0.95}Pb(I_{0.83}Br_{0.17})_3$ and $FAPbI_3(0.85)MAPbBr_3(0.15)$ perovskite by a digitizer from the references

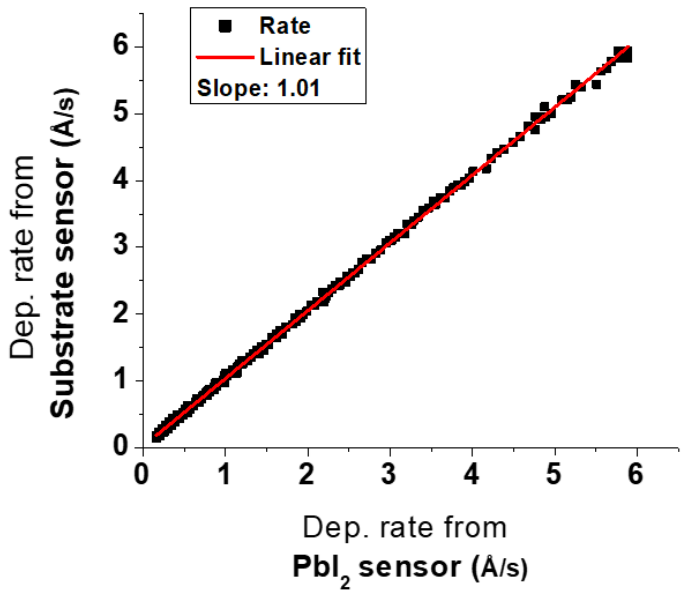

Figure S2. Rates from PbI_2 sensor *vs* Substrate sensor extracted from Fig. 1(b) and linear fitting.

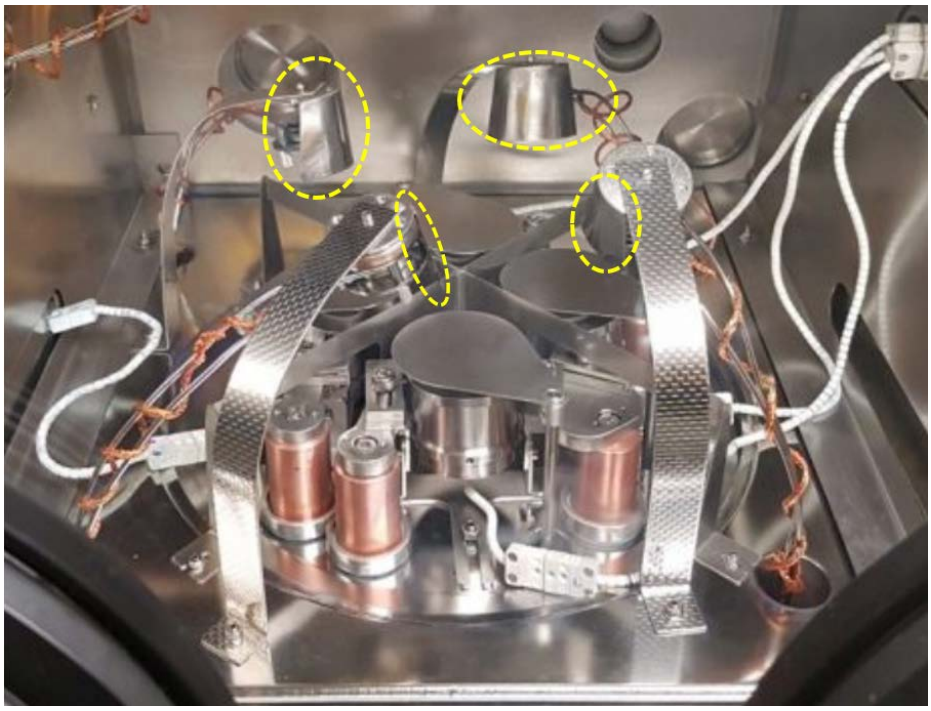

Figure S3. Photography of the inside of the evaporator. The yellow dashed lines indicate the shield of the sensors.

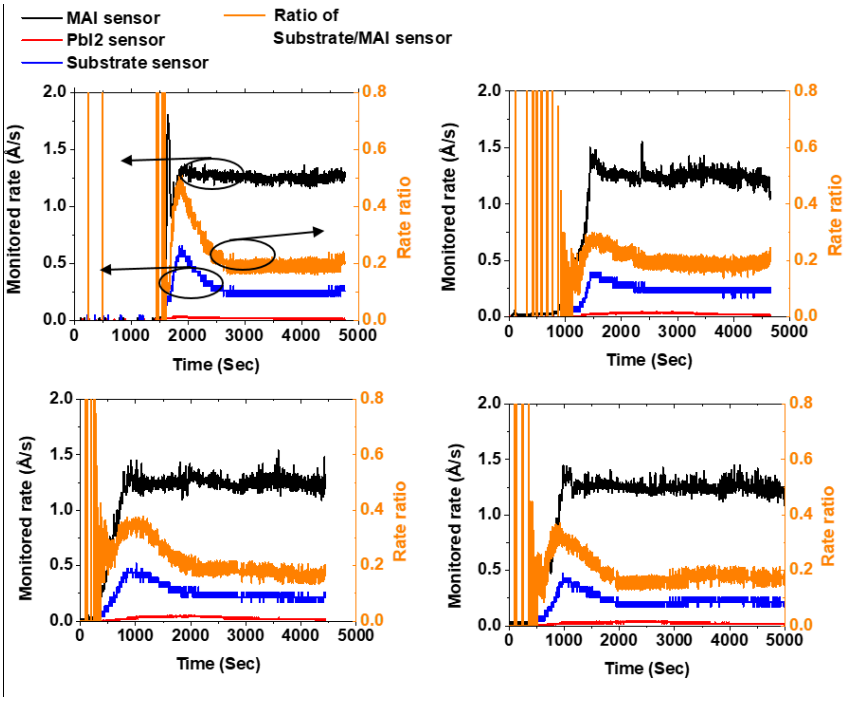

Figure S4. MAI rates from MAI sensor, Substrate sensor and their ratio with different batches of MAI.

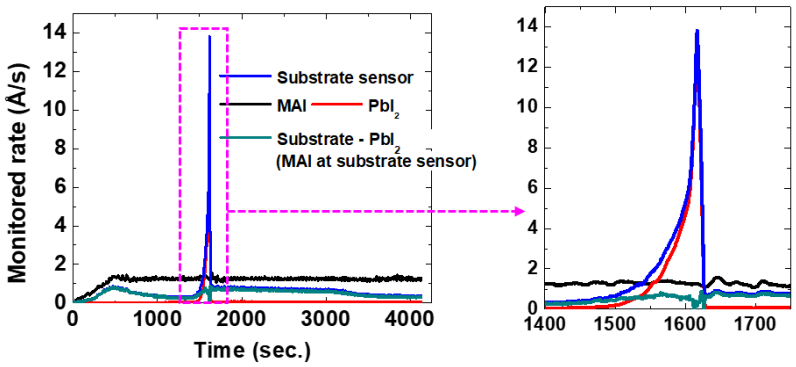

Figure S5. Deposition rates from the sensors with increased PbI_2 rates under constant MAI rate shown in Fig. 1d with full scale

Deriving the growth kinetics:

Taking into account for eqn (4) and the consideration of the surface that discussed in Fig. 3a, the $f(\theta_i)$, fractional ratio of coverage for the surface area covered by the species *i*, under the co-deposition of MAI and PbI_2 can be described as the function of the deposition rate and diffusion flux.

$$f(\theta_{MAI})=\frac{\frac{M_{MAI}}{\rho_{MAI}}r_{MAI}-\frac{M_{Perov.}}{\rho_{Perov.}}J}{\frac{M_{MAI}}{\rho_{MAI}}r_{MAI}+\frac{M_{PbI_2}}{\rho_{PbI_2}}r_{PbI_2}},\quad f(\theta_{PbI2})=\frac{\frac{M_{PbI_2}}{\rho_{PbI_2}}r_{PbI_2}-\frac{M_{Perov.}}{\rho_{Perov.}}J}{\frac{M_{MAI}}{\rho_{MAI}}r_{MAI}+\frac{M_{PbI_2}}{\rho_{PbI_2}}r_{PbI_2}},\quad f(\theta_{perov})=\frac{2\frac{M_{Perov.}}{\rho_{Perov.}}J}{\frac{M_{MAI}}{\rho_{MAI}}r_{MAI}+\frac{M_{PbI_2}}{\rho_{PbI_2}}r_{PbI_2}} \tag{S1}$$

According to Fick's first law of diffusion, *J* equals to $-D\frac{\partial c}{\partial x}$ where *D* is diffusivity, *c* is concentration and *x* is position. As shown in Fig. 3b, the thickness of the film can be represented as the distance from the substrate to the surface of the film, *x*, with time. Since we are specifically interested in *J* at the surface to reflect the change of the surface, the concentration can be replaced by the adsorption rate of MAI multiplied by time and area. Therefore, if we substitute *J* by the adsorption rate, and $f(\theta_i)$ into eqn (S1), then we obtain,

$$r_{MAI}=\varphi_{MAI}\left(S_{MAI}\frac{\frac{M_{MAI}}{\rho_{MAI}}r_{MAI}-\frac{M_{Perov.}}{\rho_{perov.}}D\,\partial r_{MAI}/\partial x\cdot A\cdot t\cdot}{\frac{M_{MAI}}{\rho_{MAI}}r_{MAI}+\frac{M_{PbI_2}}{\rho_{PbI_2}}r_{PbI_2}}+S_{PbI2}\frac{\frac{M_{PbI_2}}{\rho_{PbI_2}}r_{PbI_2}-\frac{M_{Perov.}}{\rho_{perov.}}D\,\partial r_{MAI}/\partial x\cdot A\cdot t}{\frac{M_{MAI}}{\rho_{MAI}}r_{MAI}+\frac{M_{PbI_2}}{\rho_{PbI_2}}r_{PbI_2}}+S_{perov.}\frac{2\cdot\frac{M_{Perov.}}{\rho_{perov.}}D\,\partial r_{MAI}/\partial x\cdot A\cdot t}{\frac{M_{MAI}}{\rho_{MAI}}r_{MAI}+\frac{M_{PbI_2}}{\rho_{PbI_2}}r_{PbI_2}}\right) \tag{S2}$$

As we observed from Fig. 2, we determined that $S_{MAI} < S_{PbI_2} < S_{Perov.} \approx 2.7 S_{MAI}$. Therefore, taking into account these sticking probability, the molar mass (159, 461 and 620 g/mol) and the density (2.22, 6.16 and 4.16 g/cm^3) for MAI, PbI_2 and perovskite respectively from the reported values [1-3], then eqn (S2) can be presented as below, with the substitution of $D \partial r_{MAI} / \partial x \cdot A \cdot t$ to r_{MAI}' for simplicity.

$$r_{MAI} = \varphi_{MAI} \left(\frac{S_{MAI}(r_{MAI} + 9.11 r_{MAI}') + S_{PbI_2}(1.04 r_{PbI_2} - 2.07 r_{MAI}')}{r_{MAI} + 1.04 r_{PbI_2}} \right) \quad \text{(S3)}$$

We recall that r_i and S_i are adsorption rate and sticking probability of species *i*, and , φ_{MAI} is impingement rate of MAI, and r_{MAI}' is the diffusion flux of MAI, *J*, on the surface. The diffusion of MAI is fast as deduced when discussing Fig. 2. As a result the diffusion flux *J* will be limited by the slower components, either r_{MAI} or r_{PbI_2} under the co-deposition. Therefore, there are two regimes during sublimation either $r_{PbI_2} < r_{MAI}$ or $r_{MAI} < r_{PbI_2}$. When $r_{PbI_2} < r_{MAI}$, *J* will be limited by r_{PbI_2}, so we can assume that $J = r_{PbI_2}$, and substituting *J* into eqn (S3) we obtain,

$$r_{MAI} = \varphi_{MAI} \left(\frac{S_{MAI}(r_{MAI} + 9.11 r_{PbI_2}) + S_{PbI_2}(1.04 r_{PbI_2} - 2.07 r_{PbI_2})}{r_{MAI} + 1.04 r_{PbI_2}} \right) \quad \text{(S4)}$$

The solution for r_{MAI}, as function of r_{PbI_2}, φ_{MAI} and *S* is as below.

$$r_{MAI} = \sqrt{0.27 r_{PbI_2}^{\ 2} - 1.03 r_{PbI_2} S_{PbI_2} \varphi_{MAI} + 8.59 r_{PbI_2} S_{MAI} \varphi_{MAI} + 0.25 \varphi_{MAI}^{\ 2} S_{MAI}^{\ 2}} - 0.52 r_{PbI_2} + 0.50 \varphi_{MAI} S_{MAI} \quad \text{(S5)}$$

For $r_{MAI} < r_{PbI_2}$ regime, where *J* is limited by r_{MAI} hence assuming $J = r_{MAI}$ then eqn (S3) becomes,

$$r_{MAI} = \varphi_{MAI}\left(\frac{S_{MAI}(r_{MAI}+9.11r_{MAI})+S_{PbI_2}(1.04r_{PbI_2}-2.07r_{MAI})}{r_{MAI}+1.04r_{PbI_2}}\right) \quad \text{(S6)}$$

from which the solution is the following

$$r_{MAI} = 0.005\sqrt{(104r_{PbI_2}+207S_{PbI_2}\varphi_{MAI}+1011S_{MAI}\varphi_{MAI})^2+41600r_{PbI_2}S_{PbI_2}\varphi_{MAI}} - 0.52r_{PbI_2} - 1.04S_{PbI_2}\varphi_{MAI} + 5.06S_{MAI}\varphi_{MAI} \quad \text{(S7)}$$

The equations, S5 and S7 are used in Fig. 4 for the simulation.

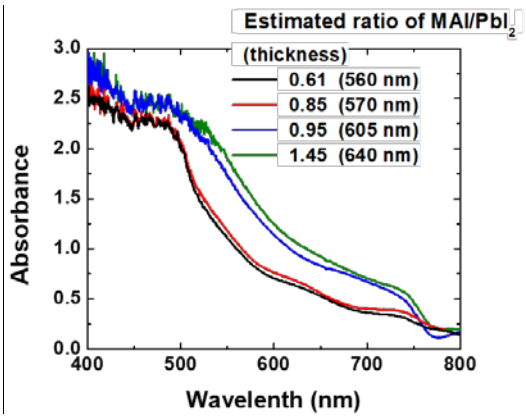

Figure S6. Absorbance and thickness of the fabricated perovskite films

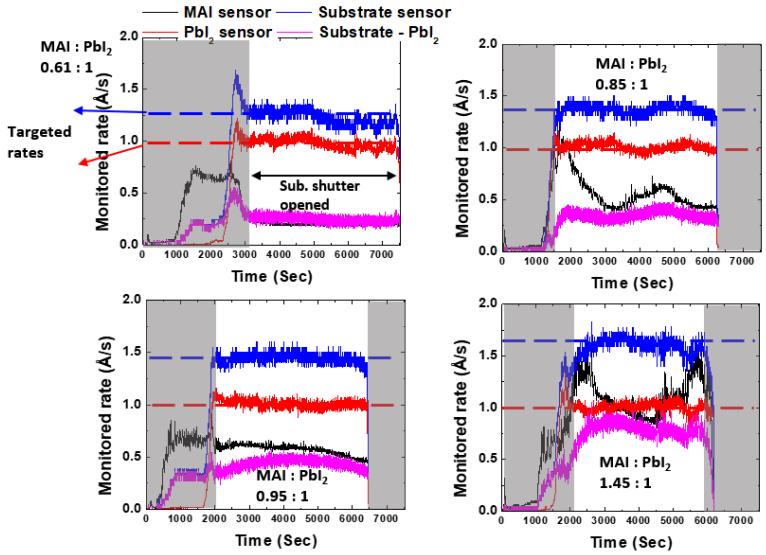

Figure S7. Recorded deposition rates changes during the MAI+PbI_2 co-deposition from different sensors with varied estimated compositions.

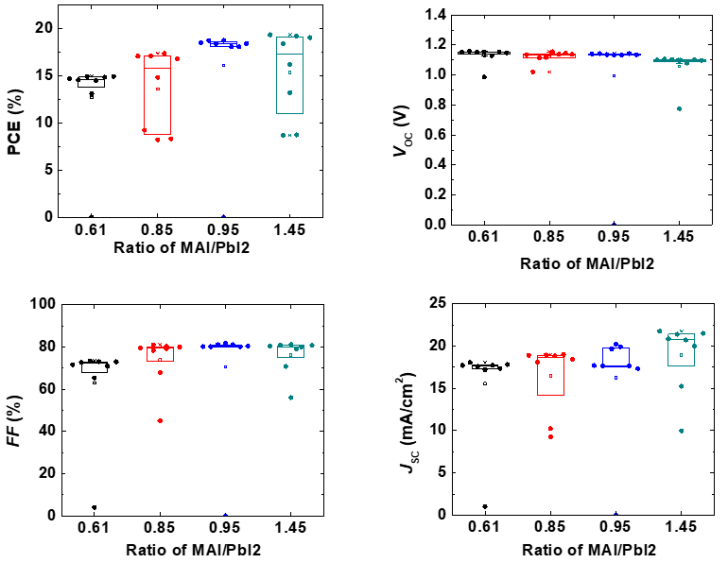

Figure S8. Photovoltaic parameters of the fabricated device measured under halogen lamp with corrected J_{SC} by convolving EQE with spectrum of AM1.5G.

References

[1] J. Teuscher, A. Ulianov, O. Müntener, M. Grätzel and N. Tétreault, *ChemSusChem*, 2015, **8**, 3847–3852.

[2] O. Yamamuro, M. Oguni, T. Matsuo and H. J. Suga, Chem. *Thermodyn*., **1986**, 18, 939.

[3] J. Huang, K. Jiang, X. Cui, Q. Zhang, M. Gao, M. Su, L. Yang and Y. *Song*, *Sci. Rep*., **2015**, 5, 15889.